



Cite this: DOI: 10.1039/c8lc01370e

# Intelligent whole-blood imaging flow cytometry for simple, rapid, and cost-effective drug-susceptibility testing of leukemia†

Hirofumi Kobayashi,<sup>id ab</sup> Cheng Lei,<sup>id \*ac</sup> Yi Wu,<sup>ad</sup> Chun-Jung Huang,<sup>ae</sup> Atsushi Yasumoto,<sup>f</sup> Masahiro Jona,<sup>f</sup> Wenxuan Li,<sup>g</sup> Yunzhao Wu,<sup>a</sup> Yaxiaer Yalikun,<sup>hi</sup> Yiyue Jiang,<sup>a</sup> Baoshan Guo,<sup>a</sup> Chia-Wei Sun,<sup>e</sup> Yo Tanaka,<sup>id h</sup> Makoto Yamada,<sup>j</sup> Yutaka Yatomi<sup>f</sup> and Keisuke Goda<sup>\*ackl</sup>

Drug susceptibility (also called chemosensitivity) is an important criterion for developing a therapeutic strategy for various cancer types such as breast cancer and leukemia. Recently, functional assays such as high-content screening together with genomic analysis have been shown to be effective for predicting drug susceptibility, but their clinical applicability is poor since they are time-consuming (several days long), labor-intensive, and costly. Here we present a highly simple, rapid, and cost-effective liquid biopsy for ex vivo drug-susceptibility testing of leukemia. The method is based on an extreme-throughput (>1 million cells per second), label-free, whole-blood imaging flow cytometer with a deep convolutional autoencoder, enabling image-based identification of the drug susceptibility of every single white blood cell in whole blood within 24 hours by simply flowing a drug-treated whole blood sample as little as 500  $\mu$ L into the imaging flow cytometer without labeling. Our results show that the method accurately evaluates the drug susceptibility of white blood cells from untreated patients with acute lymphoblastic leukemia. Our method holds promise for affordable precision medicine.

Received 15th December 2018,  
 Accepted 20th June 2019

DOI: 10.1039/c8lc01370e

rsc.li/loc

## Introduction

Leukemia is a malignancy of the body's blood-forming tissues, such as the bone marrow and lymphatic system, which results in large populations of abnormal white blood cells (WBCs). It is often difficult to cure, with a 5 year survival rate of less than 30%.<sup>1</sup> While treatment outcomes for a few types of leukemia

including chronic myeloid leukemia and acute promyelocytic leukemia have been remarkably improved by virtue of the advent of molecular targeted therapies such as imatinib<sup>2</sup> and all-trans-retinoic acid (ATRA),<sup>3</sup> treatments for other types of leukemia including acute myeloid leukemia and acute lymphoblastic leukemia (ALL) still rely on intensified use of anticancer drugs for chemotherapy<sup>4–6</sup> that often causes severe damage to organs. Consequently, treatment-related mortality rates are considerably high and the number of treatment-applicable patients is limited.<sup>7,8</sup> Meanwhile, precision medicine has become one of the most anticipated approaches to leukemia therapy in recent years for its characteristic of customizing medical treatments and practices to individual patients.<sup>9,10</sup> Genomic analysis plays a dominant role in precision medicine as it is practically the only reference available to determine the right drugs in clinical applications.<sup>11,12</sup> However, a recent study has shown that treatments based on genomic analysis are no better in progression-free survival than those based on the physician's best choice.<sup>13,14</sup> This is because therapy decisions based on genomic data are limited by scant knowledge of the complex dynamics between genotype and phenotype.<sup>15</sup> For this reason, genotype-based prediction of drug resistance or drug susceptibility with high accuracy remains as a major challenge.<sup>16–18</sup>

Direct measurement of cellular responses to anticancer drugs, known as functional assays, is an alternative means

<sup>a</sup> Department of Chemistry, University of Tokyo, Tokyo 113-0033, Japan.

E-mail: leicheng@chem.s.u-tokyo.ac.jp, goda@chem.s.u-tokyo.ac.jp

<sup>b</sup> Chan Zuckerberg Biohub, San Francisco, California 94158, USA

<sup>c</sup> Institute of Industrial Sciences, Wuhan University, Wuhan 430072, China

<sup>d</sup> Department of Computer Science, The University of Toronto, Toronto, Ontario M5S 1A1, Canada

<sup>e</sup> Department of Photonics, College of Electrical and Computer Engineering, National Chiao Tung University, Hsinchu 300, Taiwan, ROC

<sup>f</sup> Department of Clinical Laboratory Medicine, University of Tokyo, 113-8655, Japan

<sup>g</sup> Computer Science Department, Carnegie Mellon University, Pittsburgh, Pennsylvania 15213, USA

<sup>h</sup> Center for Biosystems Dynamics Research, RIKEN, Osaka 565-0871, Japan

<sup>i</sup> Division of Materials Science, Nara Institute of Science and Technology, Nara 630-0192, Japan

<sup>j</sup> Department of Intelligence Science and Technology, Kyoto University, Kyoto 606-8501, Japan

<sup>k</sup> Japan Science and Technology Agency, Kawaguchi 332-0012, Japan

<sup>l</sup> Department of Bioengineering, University of California, Los Angeles, California 90095, USA

† Electronic supplementary information (ESI) available. See DOI: 10.1039/c8lc01370e

toward precision medicine for leukemia.<sup>19–21</sup> Specifically, the combination of automated fluorescence microscopy and a compound library has opened the gateway for high-content screening (HCS),<sup>22,23</sup> by which cellular responses to drugs can be continuously monitored using fluorescence images.<sup>24</sup> Recently, HCS has been used to investigate the drug-response profiles of clinical samples from patients with leukemia.<sup>25</sup> Although the HCS approach to precision medicine for leukemia is successful as it provides molecular information, its practical utility to clinical settings is hindered by its relatively low throughput, high complexity, and high cost due to the combination of low imaging speed and the need for fluorescent labeling. Furthermore, the precision of the HCS approach is limited as it requires the enrichment of target cells by hemolysis, centrifugation, or fixation, leading to disruption of original cellular responses to drugs.

In this article, we present a highly simple, rapid, and cost-effective liquid biopsy for *ex vivo* drug-susceptibility testing (also called chemosensitivity testing) of leukemia to overcome the above limitations. The method is based on an extreme-throughput (>1 million cells per s), label-free, whole-blood imaging flow cytometer with a deep convolutional autoencoder. Consequently, it enables image-based identification of the drug susceptibility of WBCs in whole blood within 24 hours by simply flowing a drug-treated whole blood sample as little as 500  $\mu\text{L}$  into the imaging flow cytometer without labeling. Specifically, we validated the method with K562 (a human chronic myelogenous leukemia cell line) and K562/ADM (a drug-resistant strain of K562), showing the difference in their drug susceptibility *via* dose-dependent morphological changes with the same sensitivity as a conventional cell viability assay. Furthermore, we used it to accurately evaluate the drug susceptibility of WBCs from untreated ALL patients. To facilitate the interpretation of drug susceptibility for medical experts, we also demonstrated using the Hilbert–Schmidt independence criterion (HSIC)<sup>26</sup> as an index to represent the degree of drug susceptibility (ESI<sup>†</sup>). Finally, our method allowed us to quantitatively identify that leukemia cells are more vulnerable to adriamycin (a commonly used anticancer drug) than healthy cells using only the label-free images. Our results may pave the way for creating a drug susceptibility panel of all available anticancer drugs for each patient and thus providing a new diagnostic method to determine which anticancer drug is more suitable for the patient. Selecting more effective anticancer drugs in a simple, rapid, and cost-effective way can eventually improve the survival rate of leukemia patients.

## Results

### Experimental procedure

The procedure to apply our extreme-throughput whole-blood imaging flow cytometer with a deep convolutional autoencoder, or an intelligent whole-blood imaging flow cytometer in short, for simple, rapid, and cost-effective drug-susceptibility testing is shown in Fig. 1a. Specifically, a blood

sample under test is first treated with a drug, which is the only required wet experimental procedure in our method, and then imaged by the whole-blood imaging flow cytometer that is capable of acquiring single-cell images at an extremely high throughput of >1 million cells per s. Owing to this high-throughput measuring capability of the imaging flow cytometer, the blood sample can be undiluted whole blood without the need for removing red blood cells by hemolysis. Finally, a deep convolutional autoencoder is used to extract morphological features from the cell images and to produce results of their drug susceptibility.

### Whole-blood imaging flow cytometry

The whole-blood imaging flow cytometer consists of an optical time-stretch microscope and a hydrodynamic focusing microfluidic device. The optical time-stretch microscope is schematically shown in Fig. 1b. A femtosecond pulse laser with a center wavelength of 790 nm, a broad spectrum of 40 nm, a repetition rate of 75 MHz and a pulse width of about 30 fs is employed as the optical source. First, each pulse from the laser is temporally stretched according to the different transmission velocities of different wavelengths in the dispersive fiber. The temporally stretched pulse is spatially dispersed by the first diffraction grating and focused on a flowing cell in a microchannel by the first objective lens so that the one-dimensional spatial profile of the cell is mapped onto the spectrum of the pulse. The transmitted pulse is collected by the second objective lens, recombined by the second diffraction grating, detected by the photodetector, and sampled by the oscilloscope. Pulses are repeated at the pulse repetition rate of the laser while cells flow in the microchannel. Finally, the temporal waveforms of the repeated pulses are digitally segmented and stacked to form a two-dimensional image of the cell. Benefiting from the high repetition rate of the pulse laser and the single-pixel-detection scheme, the optical time-stretch microscope is able to acquire images continuously at a high line scan rate of 75 MHz. In addition to the high-speed image acquisition, a microfluidic device that supports high-speed cell flows is essential to achieve whole blood analysis. As shown in Fig. 1c, a hydrodynamic focusing channel is employed for the whole-blood imaging flow cytometer. The channel is designed to be short in height (30–40  $\mu\text{m}$ ) to achieve accurate focusing for imaging and narrow in width (80  $\mu\text{m}$ ) to achieve a high flow speed (>10  $\text{m s}^{-1}$ ). To protect the microchannel from the high pressure caused by the high-speed flow, the microchannel is designed to be narrow only in the imaging area after the merging point of the sheath and sample flows and wide in the other parts of the microchannel to relieve the overall pressure inside. A cover slip is attached on top of the device, particularly over the imaging area, to enhance its mechanical strength (Fig. S1<sup>†</sup>). As shown in Fig. 1c, the cells gradually spread out as they flow along the microchannel, enabling clear images of single cells to be acquired. Fig. 1d shows a typical image taken with the whole-blood imaging

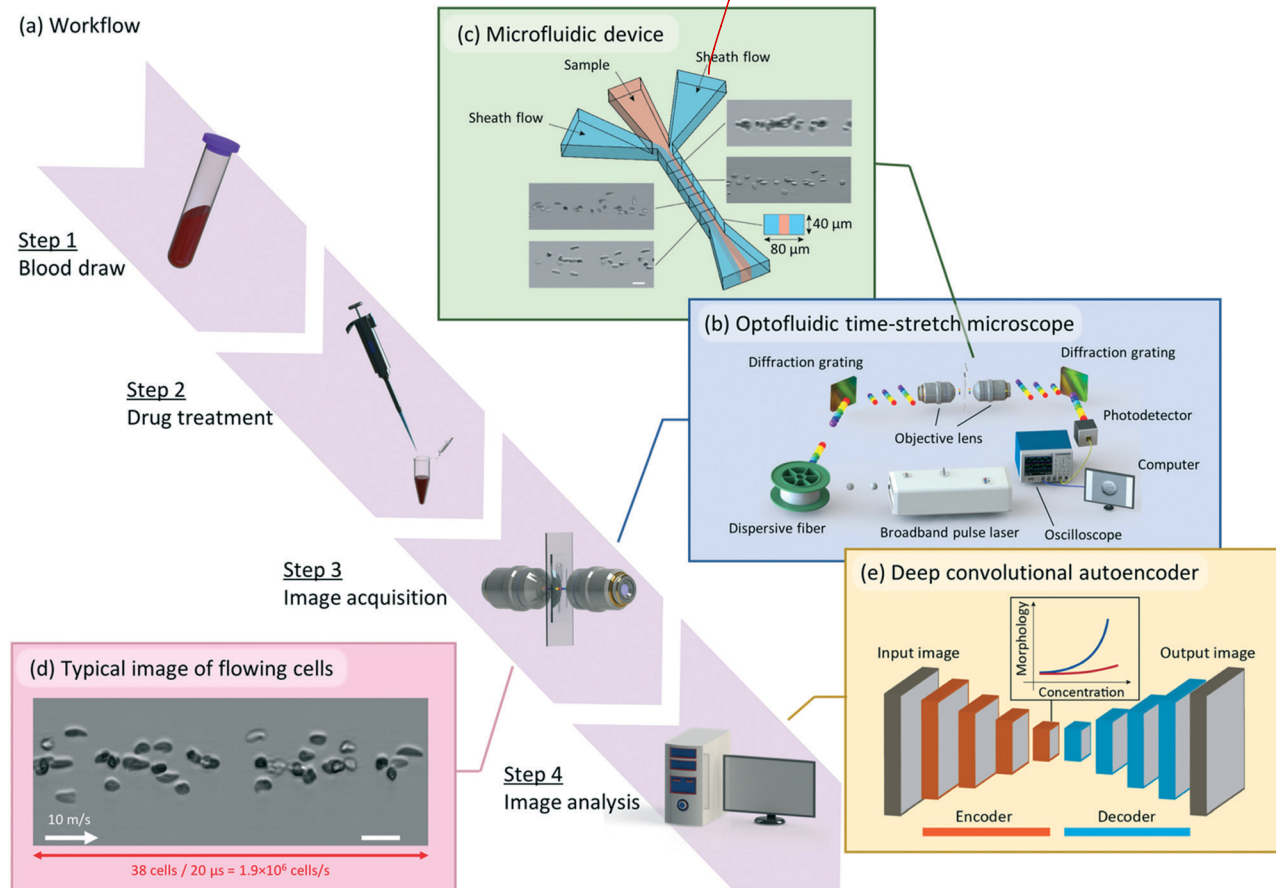


**Fig. 1** Drug-susceptibility testing with the deep whole-blood imaging flow cytometer. (a) Workflow of drug-susceptibility testing. Whole blood or cultured cells are treated with a drug to induce morphological changes. Bright-field images of the cells are obtained by the optofluidic time-stretch microscope and then analyzed using the deep convolutional autoencoder. (b) Schematic illustration of the optofluidic time-stretch microscope. (c) Schematic of the microfluidic device. The insets show images of flowing whole blood cells at different downstream locations in the central microchannel. Scale bar: 20 μm. (d) Typical image of flowing cells showing an extreme throughput of 1.9 million cells per s. Scale bar: 20 μm. (e) Schematic illustration of the deep convolutional autoencoder. Drug-induced morphological changes are investigated in the feature space at the latent layer.

flow cytometer where 38 cells were imaged within 20 μs, demonstrating an extreme throughput of >1 million cells per s.

### Deep convolutional autoencoder

To test the drug susceptibility of cells using their bright-field images, the intelligent whole-blood imaging flow cytometer employs a deep convolutional autoencoder<sup>27</sup> to extract morphological features from cell images and use them to analyze drug-induced morphological changes of the cells. Specifically, the deep convolutional autoencoder consists of two sets of deep convolutional neural networks (CNNs) functioning as an encoder and a decoder (Fig. 1e). One of the advantages of using a CNN is that it supports end-to-end learning, which means that feature data can be obtained by simply inputting cell images into the network without any prerequisite image processing such as segmentation. Another advantage of using a CNN for feature extraction over conventional methods, such as CellProfiler<sup>28,29</sup> which requires predetermination of features to be extracted, is that features to be extracted are flexi-

ble and automatically optimized to specific tasks. In our experiments, among multiple available CNN implementations, the deep convolutional autoencoder is chosen for two reasons. First, an autoencoder can learn to investigate image features in an unsupervised manner, which allows for investigation of the cells without any prior assumptions. Second, an autoencoder is more robust to noise<sup>30,31</sup> than a CNN designed only for classification tasks, because the decoder in the autoencoder acts as a regularizer to prevent the encoder from solely learning discriminative noise features. Additionally, as we demonstrate below, semi-supervised learning and classification with the autoencoder can be performed by adding a classifier on the latent space. Furthermore, with supervised learning, the structure of an autoencoder can also be applied to segmentation tasks in which multiple types of cells in one image can be segmented at a pixel-wise level (Fig. 3e).

With all the morphological features extracted by the autoencoder from the cell images, we employ two methods, namely the maximum mean discrepancy (MMD) and HSIC, to quantitatively evaluate drug-induced morphological

用MMD和HSIC来评估

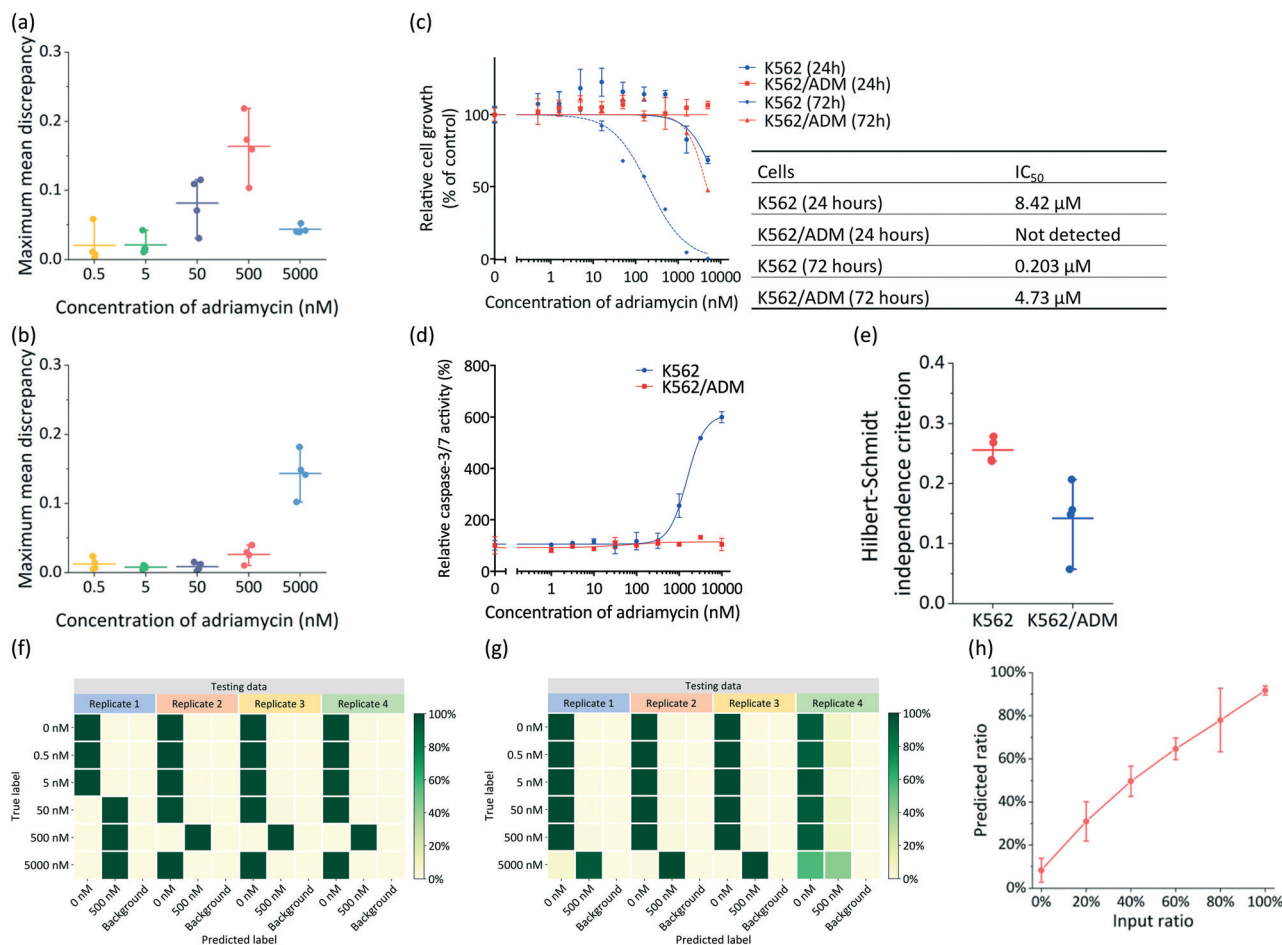


**Fig. 2** Drug-susceptibility testing of K562 and K562/ADM cells. Values of the maximum mean discrepancy (MMD), which represent the level of drug-induced morphological changes, show different responses to different concentrations of adriamycin between (a) K562 cells and (b) K562/ADM cells, indicating the difference in drug susceptibility between the two cell lines ( $n = 4$ ). (c) Growth inhibition of K562 and K562/ADM cells represented by the dose-dependence curve ( $n = 3$ ). (d) Dose-response curve of the caspase-3/7 activity of K562 and K562/ADM cells ( $n = 3$ ). (e) Hilbert-Schmidt independence criterion (HSIC) that estimates the higher-order moments between changes in drug concentration and cell morphology ( $n = 4$ ). (f) Confusion matrix of adriamycin-treated K562 cells obtained from three-class semi-supervised autoencoder models trained on three trials of K562 cells (Fig. S4b†). (g) Confusion matrix of drug-treated K562/ADM cells obtained from a three-class semi-supervised autoencoder model trained on all trials of K562 cells. Values in the confusion matrices and color bars indicate the percentage of the population of each of the true label that was classified as each of the predicted label. (h) Prediction of the composition of K562/ADM cells in the mixtures with K562 cells. The mixing ratio of K562/ADM in K562 was determined from drug-induced morphological changes. The error bars represent standard errors of the mean values.

两个随机变量的联合分布与边缘分布乘积之间

changes in a high-dimensional feature space ( $ESI^\dagger$ ). The MMD provides a nonparametric measurement of the difference between two distributions.<sup>32</sup> Specifically, MMD values between the negative control (*i.e.* untreated population) and cells treated with various concentrations of adriamycin are calculated to evaluate the drug-induced morphological changes of the drug-treated cells compared with untreated cells. In other words, at a given drug concentration, the larger the MMD value, the greater the extent of cellular morphological changes induced by the drug.<sup>33</sup> While the MMD is particularly useful in estimating the difference between two cell populations treated with different concentrations of drugs, a single index to estimate the drug susceptibility of a certain cell type across all drug concentrations can also be useful for medical experts. For this purpose, we employed an indepen-

dence measure called the HSIC, which can be interpreted as the MMD between the joint distributions and the product of margin distributions of two random variables.<sup>26</sup> In our settings, we use the HSIC to measure the dependency (potentially nonlinear) between the drug-induced morphological changes of the cells, captured by the autoencoder, and the applied drug concentration. The larger the HSIC value, the stronger the dependency of drug-induced morphological changes on the drug concentration, and thus the higher the drug susceptibility.

#### *In vitro* drug-susceptibility testing

To validate our method, we first evaluated the drug susceptibility of K562 and K562/ADM cells after a 24 hour drug



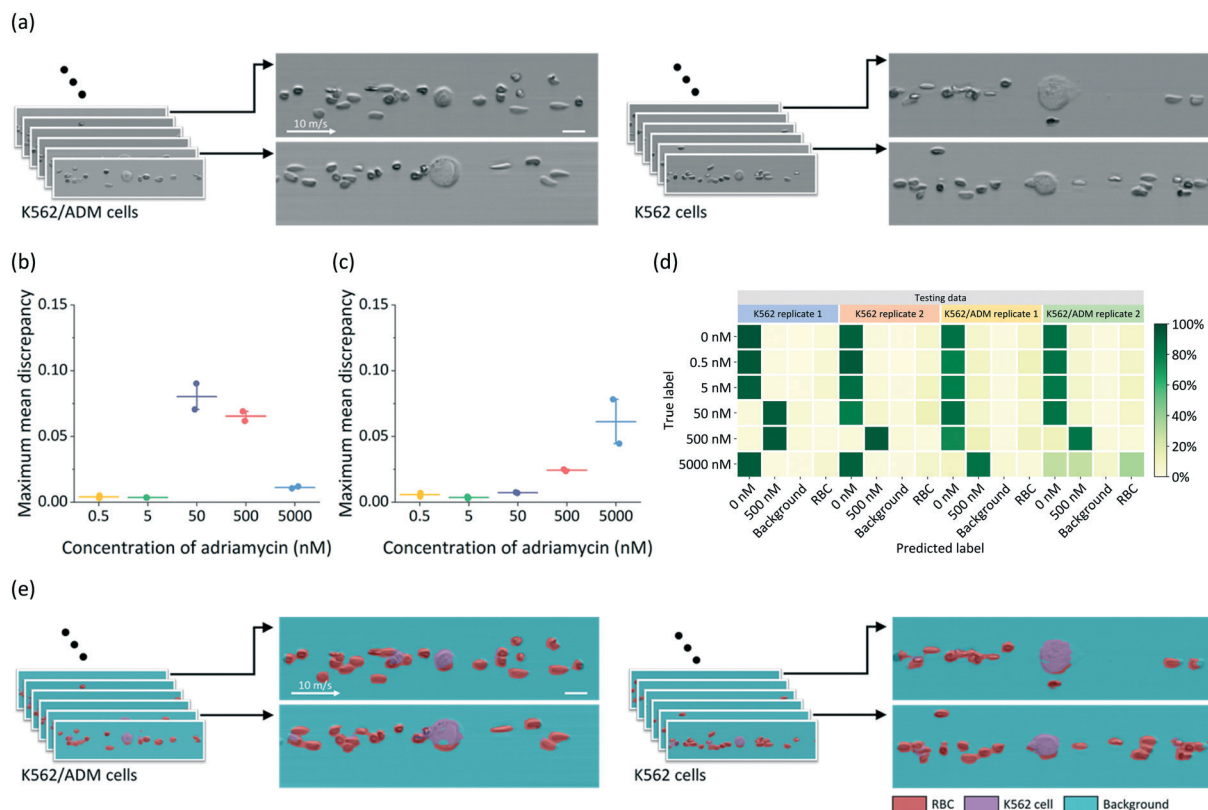


**Fig. 3** Drug-susceptibility testing of K562 and K562/ADM cells spiked in whole blood. (a) Image library of K562 and K562/ADM cells spiked in whole blood. The images were acquired with an extreme throughput of  $>1$  million cells per s. Scale bar:  $20\ \mu\text{m}$ . Dose-dependent increase in the MMD value of (b) K562 and (c) K562/ADM cells spiked in whole blood. (d) Confusion matrices of K562 and K562/ADM cells spiked in whole blood. Values in the confusion matrices and color bars indicate the percentage of the population of each true label that was classified as each predicted label. (e) Images of K562 and K562/ADM cells spiked in whole blood are segmented into K562 cells, RBCs, and the background by the deep convolutional autoencoder. The error bars represent standard errors of the mean values ( $n = 4$ ).

treatment when most of the cells were still alive. Both cell lines were treated with 6 different concentrations of adriamycin and then imaged with the intelligent whole-blood imaging flow cytometer as shown in the image libraries in Fig. S2†. About 10 000 cell images were acquired for each concentration. With four replicates of measurements for each cell line, a total number of 480 000 single-cell images were acquired. The morphological features of the cells were extracted from the cell images with the deep convolutional autoencoder into a 4608-dimensional latent space (Fig. S3a†). Note that the features were extracted in an unsupervised manner where no information regarding the drug concentration was given to the autoencoder. We employed unsupervised learning to avoid introducing biases when extracting features due to supervised classification. The drug susceptibility was evaluated by analyzing drug-induced morphological changes, which were estimated by calculating MMD values between the distributions of drug-treated and -untreated cells in the feature space (Fig. S4a†). The MMD values obtained from four experimental trials are shown in Fig. 2a and b. We found from the MMD values that the largest morphological changes (*i.e.* the largest MMD values) were detected in K562 and K562/ADM cells treated with 500 nM

and 5000 nM adriamycin, respectively, which indicates that K562 cells are more sensitive to adriamycin than K562/ADM cells. As shown in Fig. 2c, a consistent difference in the drug susceptibility of K562 and K562/ADM cells can be found in a conventional cell viability assay, in which the  $\text{IC}_{50}$  of K562/ADM cells is about 10 times higher than that of K562 cells. Our method requires only 24 hours to identify the drug susceptibility while the conventional cell viability assay requires 72 hours (three times longer) to examine the same difference, indicating our method's higher sensitivity. Furthermore, we also performed a caspase-3/7 activity assay with both cell lines after a 24 hour drug treatment to investigate whether the morphological changes were accompanied by an early stage of apoptosis. A surge of caspase-3/7 activity in K562 cells treated with  $>1000$  nM adriamycin was detected while no significant increase of caspase activity was detected in K562/ADM cells, indicating that the morphological changes occurred at a lower concentration than the increase in caspase-3/7 activity did. In other words, our method was able to sensitively detect the drug response of K562 cells at low drug concentrations where apoptosis was rarely initiated (Fig. 2d). Finally, to demonstrate the drug susceptibility of each cell line in one index, we calculated HSIC values of

K562 and K562/ADM cells (ESI†). As shown in Fig. 2e, over the four replicates of experiments, the HSIC values of K562 cells were found to be significantly higher than those of K562/ADM cells, demonstrating higher adriamycin susceptibility in K562 cells than in K562/ADM cells.

Next, to validate that our method using the deep convolutional autoencoder can precisely identify the drug-induced morphological changes that are encoded in the 4608-dimensional tensors, we examined whether the autoencoder model could stably detect the drug-induced morphological changes in K562 cells across four experimental trials. Specifically, we modified the autoencoder by adding a one-layer neural network as a classifier on top of the features (Fig. S3b†) and trained the model in a semi-supervised manner. In other words, we trained the model on the images of the negative control, K562 cells treated with 500 nM adriamycin, and on the images only with the background (the area surrounding the cell in the image), and tested the model on the K562 cells treated at all concentrations. By adding background images as an auxiliary class to be distinguished, we trained the model to learn noise-independent features. Considering that the largest morphological changes in K562 cells were detected in the group treated with 500 nM adriamycin, all the cells strongly expressing these morphological changes would be classified as “500 nM-treated cells” in all replicates, while others would be classified as “0 nM.” We performed the classification with a four-fold cross-validation: we trained the deep convolutional autoencoder with three experiments and tested it on the fourth experiment (Fig. S4b†). The calculated MMD values between the negative control and the drug-treated cells of the test set showed dose dependency consistent with the MMD values obtained from the unsupervised autoencoder models (Fig. S5a†). The confusion matrix for the additional one-layer neural network is shown in Fig. 2f, where the groups treated with 500 nM adriamycin were all accurately classified, indicating that our method was able to robustly extract the drug-induced morphological changes that were well conserved across multiple experimental trials.

To investigate whether the morphological changes that occurred in adriamycin-treated K562 cells and K562/ADM cells shared the same or similar features, we tested the above model trained with K562 cell images on the data of the four experimental trials of K562/ADM cells. High MMD values were identified in K562/ADM cells treated with 5000 nM adriamycin, which was consistent with the results obtained from the unsupervised model (Fig. S5b†). The confusion matrix in Fig. 2g shows that most of the K562/ADM cells treated with 5000 nM adriamycin were classified as “500 nM”-treated K562 cells at high instances, indicating that the drug-induced morphological changes that occurred in K562 cells and K562/ADM cells share the same or similar features, which can be detected and analyzed with a single model of the deep convolutional autoencoder.

We further investigated the capability of our method to estimate the composition of drug-resistant cells. Mixtures of

K562 and K562/ADM cells with various composition ratios were treated with 500 nM adriamycin for 24 hours following the same procedure as above to induce the largest morphological changes between K562 and K562/ADM cells. More than 4000 single-cell images per sample were then acquired by the optofluidic time-stretch microscope and fed into the deep convolutional autoencoder to predict whether each cell was a non-treated K562 cell or a K562 cell treated with 500 nM adriamycin. The results in Fig. 2h show a linear correlation between the input mixing ratio and the predicted ratio, demonstrating the capability of our method in the detection of drug-resistant cells that only depend on the drug-induced morphological changes.

### Drug-susceptibility testing of leukemia cells spiked in whole blood

Following the *in vitro* evaluation above, we used the intelligent whole-blood imaging flow cytometer to investigate cells in whole blood without dilution. Specifically, we spiked K562 or K562/ADM cells in the whole blood of a healthy donor to simulate a realistic blood sample from a leukemia patient and then evaluated whether our method could identify the drug susceptibility of K562 or K562/ADM cells by evaluating drug-induced morphological changes. About 5000 cell images were acquired at each concentration of adriamycin. With two replicates of measurements for each cell line, a total of 120 000 images were acquired at >1 million cells per s. Fig. 3a shows the images of K562 and K562/ADM cells spiked in whole blood. To test whether the morphological changes of K562 and K562/ADM cells could be detected even when the cells were outnumbered by red blood cells (RBCs) and without any cell segmentation, we trained a 4-class semi-supervised autoencoder model to distinguish K562 cells treated with 0 and 500 nM adriamycin, the background, and RBCs. Using this model, we extracted features and analyzed the images of spiked K562 and K562/ADM cells. The MMD values of the spiked K562 cells were high at 50 and 500 nM treatments while those of K562/ADM cells were high at 500 and 5000 nM treatments, demonstrating good agreement with the results of the experiments performed with K562 or K562/ADM cells alone (Fig. 3b and c). The confusion matrix shown in Fig. 3d also demonstrates a consistent agreement with the confusion matrices in Fig. 2f and g, indicating that the same morphological changes were detected in the leukemia cells spiked in whole blood.

We performed cell segmentation on the image of flowing cells at a pixel-wise level to demonstrate that the intelligent whole-blood imaging flow cytometer is also able to automatically locate target cells in an image. Specifically, we trained the segmentation model with supervised learning on the images of drug-treated and -untreated K562 cells not containing RBCs and the images of RBCs alone. By employing an Xception-like structure in the encoder<sup>34,35</sup> (Fig. S6†), we were able to segment K562 or K562/ADM cells and RBCs with an overall accuracy of 86% at the pixel level (Fig. 3e). For the

purpose of detecting K562 or K562/ADM cells in a frame, the accuracy is nearly 100%. While we showed that drug-induced morphological changes were detected through end-to-end learning, cell segmentation is useful particularly for extracting easily interpretable features such as the area, perimeter and aspect ratio, which are commonly used for image-based cell analysis.

### Ex vivo drug-susceptibility testing

Finally, we applied the intelligent whole-blood imaging flow cytometer to blood samples of leukemia patients for *ex vivo* drug-susceptibility testing of WBCs in the samples. In contrast to the cell lines, drug-induced morphological changes of WBCs in leukemia patient blood may vary from patient to patient. Furthermore, RBCs may be present with WBCs in the same image. Therefore, we extracted the features by using a three-class semi-supervised deep convolutional autoencoder, in which WBCs, RBCs, and the background were classified. Depending on the sample availability, approximately 5000 to 10000 cell images were acquired at each concentration of adriamycin. Image libraries of WBCs and leukemia cells of ALL patients and healthy donors (Table 1) are shown in Fig. 4a and b, respectively. Based on the plasma concentration of adriamycin in patients under treatment,<sup>36</sup> we treated the WBCs of ALL patients under treatment with various concentrations of adriamycin ranging from 5  $\mu\text{M}$  to 500  $\mu\text{M}$ . A dose-dependent increase of the MMD was detected in the feature space (Fig. 4c), whereas only a trivial increase at the highest concentration was detected for healthy donors (Fig. 4d). Although large variations are present in the ALL patients, the monotonic increase in the MMD is evident in the ALL patient samples. To evaluate the drug susceptibility of the WBCs of the ALL patients, the HSIC was calculated for each sample. Fig. 4e shows that the correlation between the change in morphology and the drug concentration is stronger in the ALL patients than that in the healthy donors. This result indicates that the WBCs of the ALL patients are more susceptible to adriamycin than those of healthy donors, which is reasonable because the patients did not undergo chemotherapy and hence did not develop drug resistance. This dose dependency is also consistent with the *in vitro* experiments using K562 and K562/ADM cells, where drug-susceptible cells show more evident dose-dependent changes in MMD (Fig. 2a and 3b) and higher HSIC values (Fig. 2e) than those of drug-resistant cells (Fig. 2b and 3c). Interestingly, the patient samples treated with 500  $\mu\text{M}$  adriamycin

seemingly converged to an MMD value of 0.08, suggesting that the cells were in the process of dying at this concentration. Specifically, they may have been at some point of apoptosis where the cells expressed distinctive patterns in their morphology, but not after fragmentation as we excluded apoptotic body-like objects. However, it should be noted that the MMD only indicates the relative morphological difference from non-treated cells and thus the absolute value of 0.08 does not mean that the cells were dying. In summary, we consistently demonstrated that our method was able to capture dose-dependent morphological changes that occur in drug-susceptible cells regardless of whether they are culture cells or primary blood cells.

## Discussion

In this article, we demonstrated optofluidic time-stretch microscopy of undiluted whole blood at an extremely high throughput of  $>1$  million cells per s. By processing the label-free images with a deep neural network, we quantitatively analyzed the drug susceptibility of leukemia cells. Our results with cell lines were also experimentally verified with clinical samples from leukemia patients. Furthermore, our method combined advances in deep learning with the high-throughput capability of the optofluidic time-stretch microscope to enable label-free whole-blood imaging flow cytometry. The versatility of the deep convolutional autoencoder allowed for sensitive and robust feature extraction of drug-induced morphological changes, enabling quantitative evaluation of differences in drug susceptibility of leukemia cells. The extreme throughput of the optofluidic time-stretch microscope removed the need for purifying target cells, thus making the experimental procedure simple and cost-effective. The imaging capability and label-free compatibility of our method provided richer information and broader utility than conventional methods, offering a new modality in blood diagnosis while also demonstrating the potential of label-free images in cytological analysis.

There has been a strong motivation in the quest for extreme throughput of imaging flow cytometry. Microfluidic devices aiming to acquire cell images with a high throughput of  $>1\,000\,000$  cells per s have been reported using parallelized inertial focusing channels.<sup>37</sup> The concept of this technique is to flow cells in parallel at a high density so that the whole field of view of a high-speed camera can be effectively utilized for capturing cell images. One limitation in this technique, however, is the trade-off between spatial resolution and throughput as high throughput must be achieved by a large field of view, which results in low spatial resolution for each cell image. In contrast, the spatial resolution of our whole-blood imaging flow cytometer is not limited by the throughput, while achieving the extreme throughput of  $>1$  million cells per s with a decent spatial resolution of 700 nm.<sup>38,39</sup> Another limitation in the approach of using parallelized channels is that the blood sample has to be diluted down to 1% v/v because a low flow-speed ( $\sim 0.42\text{ m s}^{-1}$ ) is required to

**Table 1** Characteristics of patients

Patient number	1	2	3
Disease type	T-ALL	T-ALL	B-ALL
Age	9	7	41
Gender	Female	Male	Male
Treatment	No	No	No
WBC count (cells per $\mu\text{L}$ )	10 000	1800	230 000
Blast count (%)	48	20	90



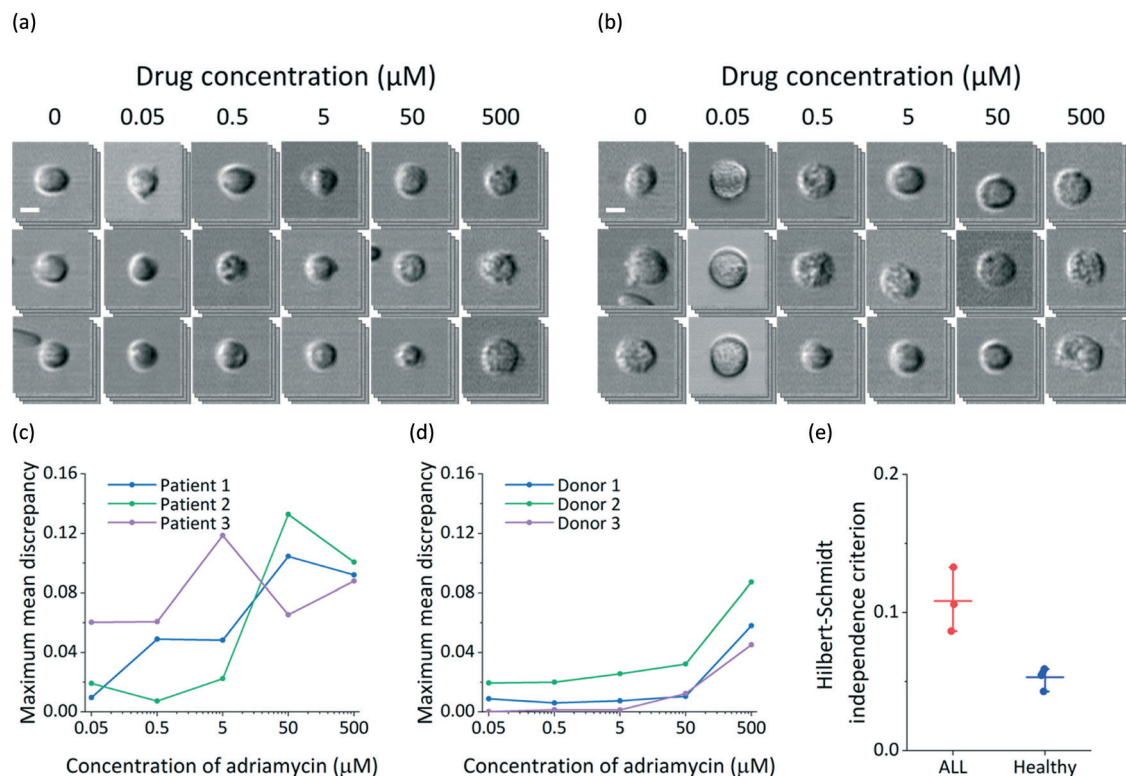


**Fig. 4** Drug-susceptibility testing of WBCs obtained from ALL patients and healthy donors. Image libraries of WBCs obtained from (a) an ALL patient and (b) a healthy donor. The images were acquired at a flow speed of  $10 \text{ m s}^{-1}$ . Scale bars:  $10 \mu\text{m}$ . (c) A dose-dependent increase in the MMD is evident for WBCs from the ALL patients through  $5 \mu\text{M}$  to  $500 \mu\text{M}$  adriamycin, whereas (d) there is only a small increase in the MMD even at the highest concentration of adriamycin for WBCs from the healthy donors. (e) Hilbert-Schmidt independence criterion (HSIC) that indicates that the correlation between changes in drug concentration and cell morphology is higher in the ALL patient blood samples than that in the healthy donor blood samples. The error bars represent standard errors of the mean values ( $n = 3$ ).

generate inertial focusing in order to align the cells at the center of each channel. In our method, the blood sample is diluted and accelerated by the sheath flows, removing the need for dilution or hemolysis.

Label-free cell images have been proven to be useful for cell classification,<sup>37,40–44</sup> cell cycle analysis,<sup>45,46</sup> and drug response detection.<sup>33</sup> Although deep learning has shown higher performance in cell classification than conventional segmentation-based approaches,<sup>40,46</sup> the application of deep learning is restricted to classification tasks. Arguably, deep learning holds greater potential for analyzing cell images than classification although it has not been fully investigated; in this study, we explored the potential of deep learning in feature extraction from cell images. Specifically, we demonstrated that a deep convolutional autoencoder was able to extract features associated with a drug treatment not only across multiple replicates, but also in a drug-resistant strain. We show that the consistent dose-dependent morphological changes (*i.e.*, increasing MMD values with increasing drug concentrations in Fig. 2a and b, Fig. 3b and c and Fig. 4c and d) appeared on both K562 and K562/ADM cells as well as on the clinical samples, but with shifted drug concentrations depending on the drug susceptibility. We also demonstrated that the ratio of drug-resistant cells among drug-susceptible cells could be estimated with our approach. To

the best of our knowledge, this is the first study that uses label-free bright-field images alone to quantitatively evaluate the drug susceptibility of leukemia cells. Furthermore, this study explores the potential of label-free images in single-cell analysis. As shown in a recent study,<sup>47</sup> pseudo fluorescence labeling on label-free transmission images can be done by deep learning, indicating that label-free images indeed contain information equivalent to fluorescence images. Given the basis provided by this work, it is of interest to visualize the features of morphological changes in a human interpretable form or elucidate the features associated with treatment with different drugs. These investigations can be done by using an extended form of the autoencoder such as a variational autoencoder<sup>27</sup> or a generative adversarial network.<sup>48</sup>

*Ex vivo* drug-susceptibility tests have been shown to have a high correlation with clinical outcomes.<sup>49</sup> In a recent study, image-based *ex vivo* drug screening using HCS for leukemia patients has been shown to be effective for predicting clinical responses.<sup>25</sup> Specifically, samples of leukemia patients were treated with anti-cancer drugs followed by immunofluorescence image analysis with an automated microscope. The patients who received treatments guided by the drug screening showed longer progression-free survival and improved overall response. In the current study, we pushed the border further by demonstrating that the drug susceptibility of leukemia



patients could be estimated by label-free images as well. Our results show the potential of label-free images for *ex vivo* drug screening and routine clinical diagnosis. Moreover, we only adopted the samples of untreated ALL patients to exclude the influence of therapeutic processes. How therapy can affect the morphology of WBCs is a future interest to translate our technique to clinical practice. Creating a database of morphological changes and associating it with therapeutic measures would help medical experts evaluate drug susceptibility against certain drugs. We anticipate that our simple, rapid and cost-effective drug-susceptibility testing can not only facilitate routine clinical investigation, but also promote the development of the database for image-based drug-susceptibility tests. Furthermore, with the recent advent of intelligent image-activated cell sorters,<sup>50</sup> it is possible to isolate those cells with certain degrees of drug susceptibility for further analysis.

## Materials and methods

### Design and fabrication of the microfluidic device

A mold of a microfluidic device was created with a negative photoresist (KMPPR1035, MicroChem) following a standard photolithography protocol. Briefly, the design of the microfluidic device was printed on a film mask. The negative photoresist was spin-coated on a silicon wafer followed by UV exposure over the film mask so that the microfluidic design was transferred onto the photoresist. Finally, the photoresist was developed, and the mold was created. A layer of polydimethylsiloxane (PDMS, Dow Corning Sylgard 184 Silicone Elastomer Kit; Ellsworth Adhesives) was developed following a standard soft lithography protocol.<sup>38</sup> In short, the PDMS was applied on the mold and baked for 15 minutes for partial curing. After 15 minutes of baking, a cover slip was placed on the top of the PDMS over the imaging area, followed by 1.5 hours of baking for complete curing. Finally, the PDMS was peeled off, punched for inlets and an outlet, and bonded to a glass slide after plasma treatment (Fig. S7†).

### Blood draw

Human blood was collected with vacuum tubes containing sodium citrate (Terumo) from healthy donors and the residual blood of leukemia patients containing EDTA (ethylenediaminetetraacetic acid, Terumo Japan) remaining after the completion of routine laboratory analyses was used. This study was approved by the Research Ethics Committee of the University of Tokyo (no. 11049-6, 11344-3). All experiments were performed in accordance with relevant laws, guidelines and regulations. Written informed consents were obtained from the healthy donors. The leukemia patients were given with the opportunity to opt out.

### Cell culture

K562 and K562/ADM cells were purchased from the JCRB cell bank. Both cells were cultured in RPMI-1640 medium (Wako

Chemicals) supplemented with 10% fetal bovine serum (MP Biomedicals) and 1% penicillin–streptomycin at 37 °C and 5% CO<sub>2</sub>. Adriamycin in a powder form (Wako Chemicals) was dissolved in dimethyl sulfoxide (DMSO, Wako Chemicals) to a stock concentration of 10 mM. One day after seeding, the cells were incubated with 10-fold serial dilutions ranging from 0.5 nM to 5 μM adriamycin. After 24 hours of incubation, cells were directly applied to the microfluidic device for imaging.

### Sample preparation

The whole blood samples were incubated with 10-fold serial dilutions ranging from 50 nM to 500 μM adriamycin for 24 hours before imaging. Due to the limited volume of leukemia patient samples, the volume of whole blood to treat with each drug concentration is less than 100 μL. Since the tubing between a syringe and the microfluidic device takes up more than 100 μL of liquid, all the blood samples were diluted 4–5 times to obtain a total sample volume of 400 μL. To ensure the image caption of WBCs, we used CD45-PE antibody (Biolegend, clone HI30) to stain WBCs. The PE was excited by a 488 nm laser and collected using a photomultiplier tube. The image acquisition was triggered by the fluorescence signal of CD45-PE to efficiently collect the images of WBCs. In the experiments where K562 or K562/ADM cells were spiked in whole blood,  $1 \times 10^6$  K562 or K562/ADM cells were treated with adriamycin for 24 hours before spiking into 1 mL of whole blood of healthy donors in each experimental trial.

### Cell viability and caspase-3/7 activity assay

K562 and K562/ADM cells were seeded in 96-well plates at  $1 \times 10^3$  cells per well one day before the drug treatment. On the following day, cells were treated with adriamycin ranging from 0.5 nM to 5000 nM. After a 24 or 72 hour treatment, a cell viability assay was performed by using CellTiter-Glo (Promega) or Caspase-Glo (Promega) following the manufacturer's protocol.

### Dataset construction and analysis

All optofluidic time-stretch microscopy images were reconstructed on MATLAB (2017a), normalized into 0 mean, and trimmed into  $190 \times 190$  pixels for K562 and K562/ADM cells and  $100 \times 100$  pixels for WBCs from the ALL patients and healthy donors. Images of debris including apoptotic body-like objects were excluded manually before feeding into an autoencoder. Deep convolutional autoencoders were implemented on Keras with the Tensorflow backbone. Image datasets were divided into training, validation, and test sets with a ratio of 3 : 1 : 1. For segmentation, images of K562 cells and RBCs were segmented on MATLAB as the ground truth. About 60 000 images of K562 cells and 10 000 images of RBCs were used to train a segmentation model. Our models learned to minimize the total loss from both supervised and unsupervised tasks,

$$L_{\text{total}} = \lambda_1 L_{\text{supervised}} + \lambda_2 L_{\text{unsupervised}}, \quad (1)$$

where  $L_{\text{supervised}}$  is the categorical cross-entropy between predicted and true labels (e.g., drug-treated and untreated cells) and  $L_{\text{unsupervised}}$  is the mean square error between input and reconstructed images. For a fully unsupervised model,  $\lambda_1 = 0$ . For a fully supervised model, such as that for the segmentation,  $\lambda_2 = 0$ . All models were optimized by Adam with an initial learning rate of 0.001. The learn rate was automatically reduced when the validation loss did not decrease for more than 3 epochs until the learning rate reached  $1 \times 10^{-8}$ . Training was terminated when the validation loss did not decrease for more than 6 epochs. A Gaussian kernel was used for both the MMD and HSIC. The kernel bandwidth was selected via the median trick.

## Author contributions

H. K. and C. L. conceived the original idea. H. K., A. Y., and M. J. performed the optical and biological experiments. H. K., Y. W., C. J. H., and W. L. analyzed the results. Y. W., Y. Y., Y. J., B. G., C. W. S., Y. T., M. Y. and Y. Y. provided assistance to the experiments and manuscript writing. H. K., C. L. and K. G. wrote the manuscript. C. L. and K. G. supervised the work. All the authors participated in revising the manuscript.

## Conflicts of interest

The authors declare no competing financial interests.

## Acknowledgements

This work was supported primarily by the ImPACT Program of the Council for Science, Technology and Innovation (Cabinet Office, Government of Japan) and partly by the JSPS Core-to-Core Program, JSPS KAKENHI Grant Number 15J02613, and White Rock Foundation. The fabrication of the microfluidic devices was conducted at the University of Tokyo's Center for Nano Lithography.

## Notes and references

- 1 B. Brinda, I. Khan, B. Parkin and H. Konig, *J. Cell. Mol. Med.*, 2018, 22, 1411–1427.
- 2 A. Hochhaus, R. A. Larson, F. Guilhot, J. P. Radich, S. Branford, T. P. Hughes, M. Baccarani, M. W. Deininger, F. Cervantes, S. Fujihara, C. E. Ortmann, H. D. Menssen, H. Kantarjian, S. G. O'Brien, B. J. Druker and I. Investigators, *N. Engl. J. Med.*, 2017, 376, 917–927.
- 3 C. C. Coombs, M. Tavakkoli and M. S. Tallman, *Blood Cancer J.*, 2015, 5, e304.
- 4 G. Ossenkoppele and B. Lowenberg, *Blood*, 2015, 125, 767–774.
- 5 H. Dohner, E. Estey, D. Grimwade, S. Amadori, F. R. Appelbaum, T. Buchner, H. Dombret, B. L. Ebert, P. Fenaux, R. A. Larson, R. L. Levine, F. Lo-Coco, T. Naoe, D. Niederwieser, G. J. Ossenkoppele, M. Sanz, J. Sierra, M. S. Tallman, H. F. Tien, A. H. Wei, B. Lowenberg and C. D. Bloomfield, *Blood*, 2017, 129, 424–447.
- 6 T. Terwilliger and M. Abdul-Hay, *Blood Cancer J.*, 2017, 7, e577.
- 7 U. Krug, C. Rolig, A. Koschmieder, A. Heinecke, M. C. Sauerland, M. Schaich, C. Thiede, M. Kramer, J. Braess, K. Spiekermann, T. Haferlach, C. Haferlach, S. Koschmieder, C. Rohde, H. Serve, B. Wormann, W. Hiddemann, G. Ehninger, W. E. Berdel, T. Buchner and C. Muller-Tidow, *Lancet*, 2010, 376, 2000–2008.
- 8 H. D. Klepin, *Hematology Am. Soc. Hematol. Educ. Program*, 2014, 2014, 8–13.
- 9 P. F. Bross, J. Beitz, G. Chen, X. H. Chen, E. Duffy, L. Kieffer, S. Roy, R. Sridhara, A. Rahman, G. Williams and R. Pazdur, *Clin. Cancer Res.*, 2001, 7, 1490–1496.
- 10 C. Lai, J. E. Karp and C. S. Hourigan, *Expert Rev. Hematol.*, 2016, 9, 1–3.
- 11 R. Kansal, *Cancer Biol. Med.*, 2016, 13, 41–54.
- 12 J. W. Tyner, *Cold Spring Harbor Mol. Case Stud.*, 2017, 3, a001370.
- 13 C. Le Tourneau, J. P. Delord, A. Goncalves, C. Gavoille, C. Dubot, N. Isambert, M. Campone, O. Tredan, M. A. Massiani, C. Mauborgne, S. Armanet, N. Servant, I. Bieche, V. Bernard, D. Gentien, P. Jezequel, V. Attignon, S. Boyault, A. Vincent-Salomon, V. Servois, M. P. Sablin, M. Kamal, X. Paoletti and S. Investigators, *Lancet Oncol.*, 2015, 16, 1324–1334.
- 14 F. Meric-Bernstam, L. Brusco, K. Shaw, C. Horombe, S. Kopetz, M. A. Davies, M. Routbort, S. A. Piha-Paul, F. Janku, N. Ueno, D. Hong, J. De Groot, V. Ravi, Y. Li, R. Luthra, K. Patel, R. Broaddus, J. Mendelsohn and G. B. Mills, *J. Clin. Oncol.*, 2015, 33, 2753–2762.
- 15 A. A. Friedman, A. Letai, D. E. Fisher and K. T. Flaherty, *Nat. Rev. Cancer*, 2015, 15, 747–756.
- 16 R. F. Schlenk, K. Dohner, J. Krauter, S. Frohling, A. Corbacioglu, L. Bullinger, M. Haddank, D. Spath, M. Morgan, A. Benner, B. Schlegelberger, G. Heil, A. Ganser, H. Dohner and G. German-Austrian Acute Myeloid Leukemia Study, *N. Engl. J. Med.*, 2008, 358, 1909–1918.
- 17 F. Pastore, A. Dufour, T. Benthous, K. H. Metzeler, K. S. Maharry, S. Schneider, B. Ksienzyk, G. Mellert, E. Zellmeier, P. M. Kakadia, M. Unterhalt, M. Feuring-Buske, C. Buske, J. Braess, M. C. Sauerland, A. Heinecke, U. Krug, W. E. Berdel, T. Buechner, B. Woermann, W. Hiddemann, S. K. Bohlander, G. Marcucci, K. Spiekermann, C. D. Bloomfield and E. Hoster, *J. Clin. Oncol.*, 2014, 32, 1586–1594.
- 18 R. B. Walter, M. Othus, E. M. Paietta, J. Racevskis, H. F. Fernandez, J. W. Lee, Z. Sun, M. S. Tallman, J. Patel, M. Gonen, O. Abdel-Wahab, R. L. Levine and E. H. Estey, *Leukemia*, 2015, 29, 2104–2107.
- 19 R. Pieters, D. R. Huismans, A. H. Loonen, K. Hahlen, A. van der Does-van den Berg, E. R. van Wering and A. J. Veerman, *Lancet*, 1991, 338, 399–403.
- 20 J. W. Tyner, W. F. Yang, A. Bankhead, 3rd, G. Fan, L. B. Fletcher, J. Bryant, J. M. Glover, B. H. Chang, S. E. Spurgeon, W. H. Fleming, T. Kovacsovich, J. R. Gotlib, S. T. Oh, M. W. Deininger, C. M. Zwaan, M. L. Den Boer, M. M. van den

- Heuvel-Eibrink, T. O'Hare, B. J. Druker and M. M. Loriaux, *Cancer Res.*, 2013, 73, 285–296.
- 21 T. Pemovska, M. Kontro, B. Yadav, H. Edgren, S. Eldfors, A. Sz wajda, H. Almusa, M. M. Bespalov, P. Ellonen, E. Elonen, B. T. Gjertsen, R. Karjalainen, E. Kuleskiy, S. Lagstrom, A. Lehto, M. Lepisto, T. Lundan, M. M. Majumder, J. M. Marti, P. Mattila, A. Murumagi, S. Mustjoki, A. Palva, A. Parsons, T. Pirttinen, M. E. Ramet, M. Suvela, L. Turunen, I. Vastrik, M. Wolf, J. Knowles, T. Aittokallio, C. A. Heckman, K. Porkka, O. Kallioniemi and K. Wennerberg, *Cancer Discovery*, 2013, 3, 1416–1429.
  - 22 Z. E. Perlman, M. D. Slack, Y. Feng, T. J. Mitchison, L. F. Wu and S. J. Altschuler, *Science*, 2004, 306, 1194–1198.
  - 23 L. H. Loo, L. F. Wu and S. J. Altschuler, *Nat. Methods*, 2007, 4, 445–453.
  - 24 Z. Yin, A. Sadok, H. Sailem, A. McCarthy, X. Xia, F. Li, M. A. Garcia, L. Evans, A. R. Barr, N. Perrimon, C. J. Marshall, S. T. C. Wong and C. Bakal, *Nat. Cell Biol.*, 2013, 15, 860–871.
  - 25 B. Snijder, G. I. Vladimer, N. Krall, K. Miura, A. S. Schmolke, C. Kornauth, O. Lopez de la Fuente, H. S. Choi, E. van der Kouwe, S. Gultekin, L. Kazianka, J. W. Bigenzahn, G. Hoermann, N. Prutsch, O. Merkel, A. Ringler, M. Sabler, G. Jerczynski, M. E. Mayerhoefer, I. Simonitsch-Klupp, K. Ocko, F. Felberbauer, L. Mullauer, G. W. Prager, B. Korkmaz, L. Kenner, W. R. Sperr, R. Kralovics, H. Gisslinger, P. Valent, S. Kubicek, U. Jager, P. B. Staber and G. Superti-Furga, *Lancet Haematol.*, 2017, 4, e595–e606.
  - 26 A. Gretton, O. Bousquet, A. Smola and B. Schölkopf, *Measuring statistical dependence with Hilbert-Schmidt norms*, Singapore, 2005.
  - 27 D. P. Kingma and M. Welling, 2013, arXiv preprint arXiv:1312.6114.
  - 28 L. Kametsky, T. R. Jones, A. Fraser, M.-A. Bray, D. J. Logan, K. L. Madden, V. Ljosa, C. Rueden, K. W. Eliceiri and A. E. Carpenter, *Bioinformatics*, 2011, 27, 1179–1180.
  - 29 A. E. Carpenter, T. R. Jones, M. R. Lamprecht, C. Clarke, I. H. Kang, O. Friman, D. A. Guertin, J. H. Chang, R. A. Lindquist, J. Moffat, P. Golland and D. M. Sabatini, *Genome Biol.*, 2006, 7, R100.
  - 30 P. Vincent, H. Larochelle, I. Lajoie, Y. Bengio and P. A. Manzagol, *J. Mach. Learn. Res.*, 2010, 11, 3371–3408.
  - 31 P. Vincent, H. Larochelle, Y. Bengio and P. A. Manzagol, *Extracting and composing robust features with denoising autoencoders*, Helsinki, Finland, 2008.
  - 32 A. Gretton, K. M. Borgwardt, M. J. Rasch, B. Schölkopf and A. Smola, *J. Mach. Learn. Res.*, 2012, 13, 723–773.
  - 33 H. Kobayashi, C. Lei, Y. Wu, A. Mao, Y. Jiang, B. Guo, Y. Ozeki and K. Goda, *Sci. Rep.*, 2017, 7, 12454.
  - 34 L. C. Chen, Y. Zhu, G. Papandreou, F. Schroff and H. Adam, 2018, arXiv preprint arXiv:1802.02611.
  - 35 F. Chollet, *Xception: deep learning with depthwise separable convolutions*, Honolulu, USA, 2017.
  - 36 D. R. Barpe, D. D. Rosa and P. E. Froehlich, *Eur. J. Pharm. Sci.*, 2010, 41, 458–463.
  - 37 S. C. Hur, H. T. Tse and D. Di Carlo, *Lab Chip*, 2010, 10, 274–280.
  - 38 C. Lei, H. Kobayashi, Y. Wu, M. Li, A. Isozaki, A. Yasumoto, H. Mikami, T. Ito, N. Nitta, T. Sugimura, M. Yamada, Y. Yatomi, D. Di Carlo, Y. Ozeki and K. Goda, *Nat. Protoc.*, 2018, 13, 1603–1631.
  - 39 C. Lei, B. Guo, Z. Cheng and K. Goda, *Appl. Phys. Rev.*, 2016, 3, 011102.
  - 40 C. L. Chen, A. Mahjoubfar, L.-C. Tai, I. K. Blaby, A. Huang, K. R. Niazi and B. Jalali, *Sci. Rep.*, 2016, 6, 21471.
  - 41 B. Guo, C. Lei, Y. Wu, H. Kobayashi, T. Ito, Y. Yalikul, S. Lee, A. Isozaki, M. Li, Y. Jiang, A. Yasumoto, D. Di Carlo, Y. Tanaka, Y. Yatomi, Y. Ozeki and K. Goda, *Methods*, 2018, 136, 116–125.
  - 42 Y. Jiang, C. Lei, A. Yasumoto, H. Kobayashi, Y. Aisaka, T. Ito, B. Guo, N. Nitta, N. Kutsuna, Y. Ozeki, A. Nakagawa, Y. Yatomi and K. Goda, *Lab Chip*, 2017, 17, 2426–2434.
  - 43 B. Guo, C. Lei, H. Kobayashi, T. Ito, Y. Yalikul, Y. Jiang, Y. Tanaka, Y. Ozeki and K. Goda, *Cytometry, Part A*, 2017, 91, 494–502.
  - 44 C. Lei, T. Ito, M. Ugawa, T. Nozawa, O. Iwata, M. Maki, G. Okada, H. Kobayashi, X. Sun, P. Tiamsak, N. Tsumura, K. Suzuki, D. Di Carlo, Y. Ozeki and K. Goda, *Biomed. Opt. Express*, 2016, 7, 2703–2708.
  - 45 T. Blasi, H. Hennig, H. D. Summers, F. J. Theis, J. Cerveira, J. O. Patterson, D. Davies, A. Filby, A. E. Carpenter and P. Rees, *Nat. Commun.*, 2016, 7, 10256.
  - 46 P. Eulenberg, N. Kohler, T. Blasi, A. Filby, A. E. Carpenter, P. Rees, F. J. Theis and F. A. Wolf, *Nat. Commun.*, 2017, 8, 463.
  - 47 E. M. Christiansen, S. J. Yang, D. M. Ando, A. Javaherian, G. Skibinski, S. Lipnick, E. Mount, A. O'Neil, K. Shah, A. K. Lee, P. Goyal, W. Fedus, R. Poplin, A. Esteva, M. Berndl, L. L. Rubin, P. Nelson and S. Finkbeiner, *Cell*, 2018, 173, 792–803e719.
  - 48 I. Goodfellow, J. Pouget-Abadie, M. Mirza, B. Xu, D. Warde-Farley, S. Ozair, A. Courville and Y. Bengio, *Generative adversarial nets*, Montreal, Canada, 2014.
  - 49 K. Blom, P. Nygren, R. Larsson and C. R. Andersson, *SLAS Technol.*, 2017, 22, 306–314.
  - 50 N. Nitta, T. Sugimura, A. Isozaki, H. Mikami, K. Hiraki, S. Sakuma, T. Iino, F. Arai, T. Endo, Y. Fujiwaki, H. Fukuzawa, M. Hase, T. Hayakawa, K. Hiramatsu, Y. Hoshino, M. Inaba, T. Ito, H. Karakawa, Y. Kasai, K. Koizumi, S. Lee, C. Lei, M. Li, T. Maeno, S. Matsusaka, D. Murakami, A. Nakagawa, Y. Oguchi, M. Oikawa, T. Ota, K. Shiba, H. Shintaku, Y. Shirasaki, K. Suga, Y. Suzuki, N. Suzuki, Y. Tanaka, H. Tezuka, C. Toyokawa, Y. Yalikul, M. Yamada, M. Yamagishi, T. Yamano, A. Yasumoto, Y. Yatomi, M. Yazawa, D. Di Carlo, Y. Hosokawa, S. Uemura, Y. Ozeki and K. Goda, *Cell*, 2018, 175, 266–276.e213.